nature communications

Article

https://doi.org/10.1038/s41467-025-56209-x

Dual-channel near-field holographic MIMO communications based on programmable digital coding metasurface and electromagnetic theory

Received: 7 April 2024

Accepted: 9 January 2025

Rui Wen Shao[1,2,6], Jun Wei Wu[1,2,3,4,6], Jiachen Li[5,6], Shengguo Meng[5], Yifan Xu[5], Zheng Xing Wang[1,2], Wankai Tang[5], Qiang Cheng[1,2], Shi Jin[5] ✉ & Tie Jun Cui[1,2,3,4] ✉

Holographic multiple-input multiple-output (MIMO) method leverages spatial diversity to enhance the performance of wireless communications and is expected to be a key technology enabling for high-speed data services in the forthcoming sixth generation (6G) networks. However, the antenna array commonly used in the traditional massive MIMO cannot meet the requirements of low cost, low complexity and high spatial resolution simultaneously, especially in higher frequency bands. Hence it is important to achieve a feasible hardware platform to support theoretical study of the holographic MIMO communications. Here, we propose a near-field holographic MIMO communication architecture based on programmable digital coding metasurface (PDCM) and electromagnetic theory. The orthogonal holographic patterns on the transmitting and receiving apertures are firstly obtained using the Hilbert-Schmidt decomposition of the radiation operator. Then the information to be transmitted is pre-encoded on PDCM following the principle of direct digital modulations. A PDCM-based holographic MIMO prototype is designed and experimentally verified in microwave frequencies. The measured results of constellations show that the prototype can realize dual-channel signal transmissions under quadrature-phase shift keying scheme. The proposed paradigm features low complexity, low cost and low power consumption, and may become a valuable technique in beyond fifth generation and 6G wireless communications.

Future wireless networks, namely beyond fifth-generation (B5G) and sixth-generation (6G) wireless communications, are expected to support massive numbers of users with remarkable spectral and energy efficiencies through high-integration, low-cost and low-power-consumption devices and systems[1–4]. The research on massive multiple-input multiple-output (MIMO) communication has attracted great attention in the wireless community. This technique exploits spatial diversity using large-scale phased arrays with high directional

---

[1]Institute of Electromagnetic Space, Southeast University, Nanjing, China. [2]State Key Laboratory of Millimeter Waves, Southeast University, Nanjing, China. [3]Peng Cheng Laboratory, Shenzhen, Guangdong, China. [4]Pazhou Laboratory (Huangpu), Guangzhou, Guangdong, China. [5]National Mobile Communications Research Laboratory, Southeast University, Nanjing, China. [6]These authors contributed equally: Rui Wen Shao, Jun Wei Wu, Jiachen Li.
✉e-mail: jinshi@seu.edu.cn; tjcui@seu.edu.cn

beam-forming capability and is considered as one of the powerful solutions to realize the challenging vision of the 6G communications. In recent years, holographic MIMO theory, which features spatially continuous apertures and fields, is introduced to surpass the massive MIMO technologies. Holographic MIMO surfaces have the huge potential to enhance spectral and energy efficiency through dynamic control of electromagnetic waves[5–8].

The current research on the holographic MIMO can be classified into two types: the first type is known as holographic beamforming, wherein the continuous current apertures are used to increase the power of received signal[7,8]; while the second type is known as holographic communication, where the continuous current aperture induces diverse spatial modes of fields that carry the symbols to be transmitted. The second type is closely related to the spatial bandwidth and degree of freedom (DoF) of electromagnetic (EM) fields[9,10], which are the bases of electromagnetic information theory (EIT). The limit of communication capacity of the holographic MIMO systems has also been reported in many studies[9–20]. From the perspective of wireless communications, DoF represents the maximum number of spatial channels that can be supported by the antenna aperture. Based on the Kolmogorov entropy and Hilbert-Schmidt decomposition, the communication capacity of the holographic MIMO has been studied for various situations, including near field[18], mutual coupling[19], and inhomogeneous medium[20].

However, the above studies on the holographic MIMO have remained at the theoretical level. The main reason is that the continuous apertures and currents cannot be realized practically due to the restriction of EM laws. Instead, they can only be approximated by using antennas with fine spatial resolution. In fact, the elements of the traditional antenna arrays can only be spaced by slightly less than half wavelength, which is far from the continuous assumption of the holographic MIMO. If the spatial interval is further reduced, the number of antenna elements and microwave components will increase rapidly, leading to high complexity, high power consumption, and high cost. Moreover, the mutual coupling between antenna elements will increase as the element period decreases, deteriorating the system performance. Although some techniques can reduce the mutual coupling, they will also increase the complexity of the system. Besides the smaller element interval, the increasing communication frequency also limits the development of holographic MIMO based on the antenna array. To sum up, it is difficult and unfeasible to realize the holographic MIMO directly by reducing the element interval of the traditional antenna array.

It is encouraging to note that the recent research on digital coding metasurfaces has provided a low-cost and low-complexity solution for holographic MIMO technologies[21–33]. The digital elements consist of passive structures and tunable devices, such as positive-intrinsic-negative (PIN) diodes, varactors, and micro electromechanical systems (MEMS). By controlling the digital voltages, the elements provide flexible manipulations on the magnitudes and phases of the EM fields on subwavelength scale. Many prototypes of holographic beamforming systems have been fabricated and experimentally measured using the coding metasurface as the main component. This architecture is also known as holographic reconfigurable intelligent surface (RIS). Multi-functional RISs with beam steering, polarization transformation, and frequency conversion pave the way for more intelligent, flexible, and efficient wireless systems[34–45].

Another architecture is known as programmable digital coding metasurface (PDCM). Specifically, the PDCM elements vary with time, and the scattered field is a mixture of the incident wave and baseband signals[46–61]. Consequently, the EM waves are modulated in both time and spatial domains, which greatly increases the degree of freedom of the wireless systems. PDCM saves lots of active components compared with the traditional MIMO systems, thus reducing the cost, complexity, and power consumption. At the same time, PDCM controls the spatial EM fields on the sub-wavelength scale, being closer to the continuous current aperture than the half-wavelength antenna array. Therefore, PDCM is an ideal candidate to fully exploit the limitation of the holographic MIMO under the guidance of EIT. However, the current research in this area is still in the theoretical stage, and there is no practical verification system.

In this article, we propose to construct a holographic MIMO communication system by using PDCM. The schematic diagram of the proposed PDCM-based holographic MIMO system is shown in Fig. 1, in which the transmitter is composed of PDCM and a field programmable gate array (FPGA). Firstly, orthogonal holographic patterns are obtained by Hilbert-Schmidt decomposition of free-space radiation operator under the guidance of EIT. Then, FPGA pre-encodes the baseband signals by the orthogonal holographic patterns and generates the control voltages for PDCM, which attaches the information to the carrier and radiates to free space. A similar procedure is adopted at the receiver, and the signal symbols are recovered by calculating the inner product of the received aperture field and the orthogonal basis patterns. A prototype is designed and fabricated in the microwave frequency. To verify the multi-channel communication capability of the proposed PDCM-based holographic MIMO system, experiments are carried out in an indoor environment. The measurements indicate that the holographic MIMO system can realize dual-channel signal transmissions under the quadrature phase shift keying (QPSK) scheme. Despite the limited performance of hardware, the experiments still show great potentials of PDCM in revealing the holographic MIMO communications. We hope that our design provides a feasible and practical route to meet the extreme requirements of B5G and 6G communication systems.

Results

Principle of holographic MIMO

As shown in Fig. 2a, the transmitter and receiver in the wireless communication system can be equivalent to two closed surfaces denoted as S_t and S_r, respectively, where the subscripts t and r represent the transmitter and receiver, respectively. A continuous current distribution $\mathbf{J}(\mathbf{r}')$ is generated onS_t, and the communication is considered to recover $\mathbf{J}(\mathbf{r}')$ through the electric fields $\mathbf{E}(\mathbf{r})$ on S_r. In this process, different current distributions are mapped to various symbols. Based on the EM wave theory, $\mathbf{E}(\mathbf{r})$ is the convolution of $\mathbf{J}(\mathbf{r}')$ and the dyadic Green's function $\overline{\mathbf{G}}(\mathbf{r},\mathbf{r}')$

$$\mathbf{E}(\mathbf{r}) = \iint_{\mathrm{S}_t} \overline{\mathbf{G}}(\mathbf{r},\mathbf{r}')\cdot\mathbf{J}(\mathbf{r}')\mathrm{ds} \tag{1}$$

where $\mathbf{r}'$ and $\mathbf{r}$ represent the position vectors on S_t and S_r, respectively. The convolution process in Eq. (1) can be denoted as a radiation operator A: $\mathrm{S}_t \to \mathrm{S}_r$ acting on $\mathbf{J}(\mathbf{r}')$

$$\mathbf{E}(\mathbf{r}) = \mathrm{A}\mathbf{J}(\mathbf{r}') \tag{2}$$

Since the operator A is a linear bounded compact operator from S_t to S_r, its singular value system$\{\sigma_n; u_n, \upsilon_n\}_{n=0}^{\infty}$ can be obtained by the Hilbert-Schmidt decomposition, yielding a combination of orthogonal basis functions in both the range and domain of the operator. Consequently,

$$\sigma_n u_n(\mathbf{r}) = \mathrm{A}\upsilon_n(\mathbf{r}') \tag{3}$$

$$\sigma_n \upsilon_n(\mathbf{r}') = \mathrm{A}^+ u_n(\mathbf{r}) \tag{4}$$

where A^+ is the adjoint operator of A; $\{u_n\}_{n=0}^{\infty}$ represents a set of orthonormal basis functions of the value domain of A, while $\{\upsilon_n\}_{n=0}^{\infty}$ forms a set of orthonormal basis functions of the closure of the range of A. As far as the singular values of A are concerned, we will observe that they have a step-like behavior, and the position of the inflection

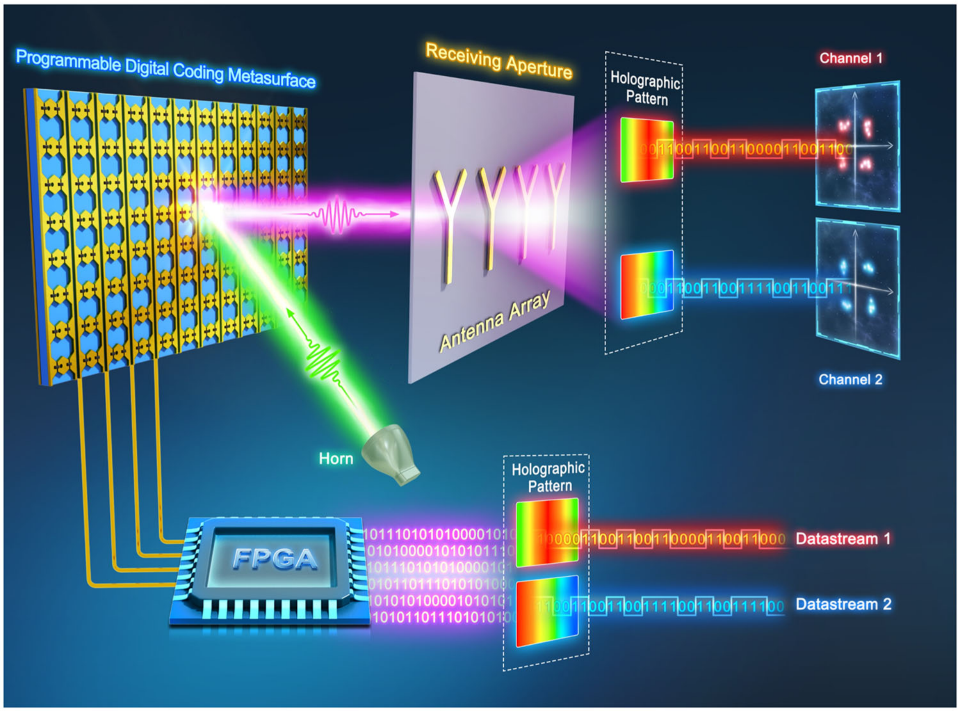

Fig. 1 | Schematic diagram of the proposed holographic MIMO system based on PDCM and EIT. The transmitter is composed of PDCM and FPGA. Firstly, orthogonal holographic patterns are obtained by the Hilbert-Schmidt decomposition of the free-space radiation operator and EIT. Then, the FPGA pre-encodes the baseband signals by the orthogonal holographic patterns and generates the control voltages for PDCM, which attaches the information to the carrier and radiates to free space. A similar procedure is adopted at the receiver, and the signal symbols are recovered by calculating the inner product of the received aperture field and the orthogonal basis patterns.

point is called as the effective degree of freedom (EDoF)[10]. In fact, EDoF is denoted asN_{EDoF} and is defined as

$$N_{\mathrm{EDoF}} = \frac{\left(\sum_{n=0}^{\infty}\sigma_n\right)^2}{\sum_{n=0}^{\infty}{\sigma_n}^2} \tag{5}$$

This makes it possible to approximate each radiated field in a finite-dimensional space spanned by the N_{EDoF} left singular functions. The singular value system of the radiation operator can provide numerous groups of current-field patterns that are orthogonal both on the receiving and transmitting apertures. Thanks to this orthogonal capability, each pattern corresponds to a spatial channel and can be used to realize multi-channel holographic communications, and the information imposed on them is independent of each other.

In this work, a simple case of two-dimensional and single-polarization holographic MIMO communication is considered. The schematic diagram of the system is shown in Fig. 2b, in which the transmitting and receiving apertures are parallel to the x-axis, and only the x-components of the current and electric field are transmitted and received. Consequently, Eq. (1) is simplified into

$$\mathrm{E}_x(x) = \int_{-a'}^{a'} \mathrm{g}(x - x', \mathrm{z}_0) J_x(x') dx' \tag{6}$$

where $g(x - x', z_0)$ is a two-dimensional scalar Green's function, a and a' represent half sizes of the receiving and transmitting apertures, respectively, and z_0 is the distance between them. In this case, the EDoF of the system has a semi-analytical expression[10]

$$N_{\mathrm{EDoF}} = \frac{2\left[\sqrt{(a+a')^2 + z^2} - \sqrt{(a-a')^2 + z^2}\right]}{\lambda} \tag{7}$$

Supposing that there are N independent baseband signals denoted as $s_1(t), s_2(t), \ldots, s_N(t)$, respectively, the nth signal can be attached to the nth current pattern. Consequently, we multiply $s_n(t)$ and $\upsilon_n(x')$, and then accumulate the products to obtain the total current distribution on the transmitting aperture

$$\mathrm{J}_x(x', t) = \sum_{n=1}^{N} \upsilon_n(x') s_n(t) \tag{8}$$

As the EM wave propagates, the electric field on the receiving aperture is

$$\mathrm{E}_x(x, t) = \mathrm{A}\,\mathrm{J}_x(x', t) = \sum_{n=1}^{N} \sigma_n u_n(x) s_n(t) \tag{9}$$

Because of the orthogonal feature of the singular value system, the mth signal is obtained by calculating the inner product of the received field and the mth pattern $u_m(x)$, namely

$$\int_{-a}^{a} {u_m}^*(x)\mathrm{E}_x(x, t)dx = \sum_{n=1}^{N} \sigma_n s_n(t) \int_{-a}^{a} {u_m}^*(x) u_n(x) dx = \sigma_m s_m(t) \tag{10}$$

It can be found from Eq. (10) that the proposed system can realize lossless information transmissions theoretically, and the channel gain is σ_m. However, various noises and interferences in the communication process make the channels with small gains unusable. Because σ_m has a step-like behavior and the first N_{EDoF} singular values are much larger than the others, the number of channels available for communication is actually N_{EDoF}.

PDCM-based holographic MIMO

In this communication scheme, the channel information can be obtained by calculation under the guidance of EIT, which eliminates the

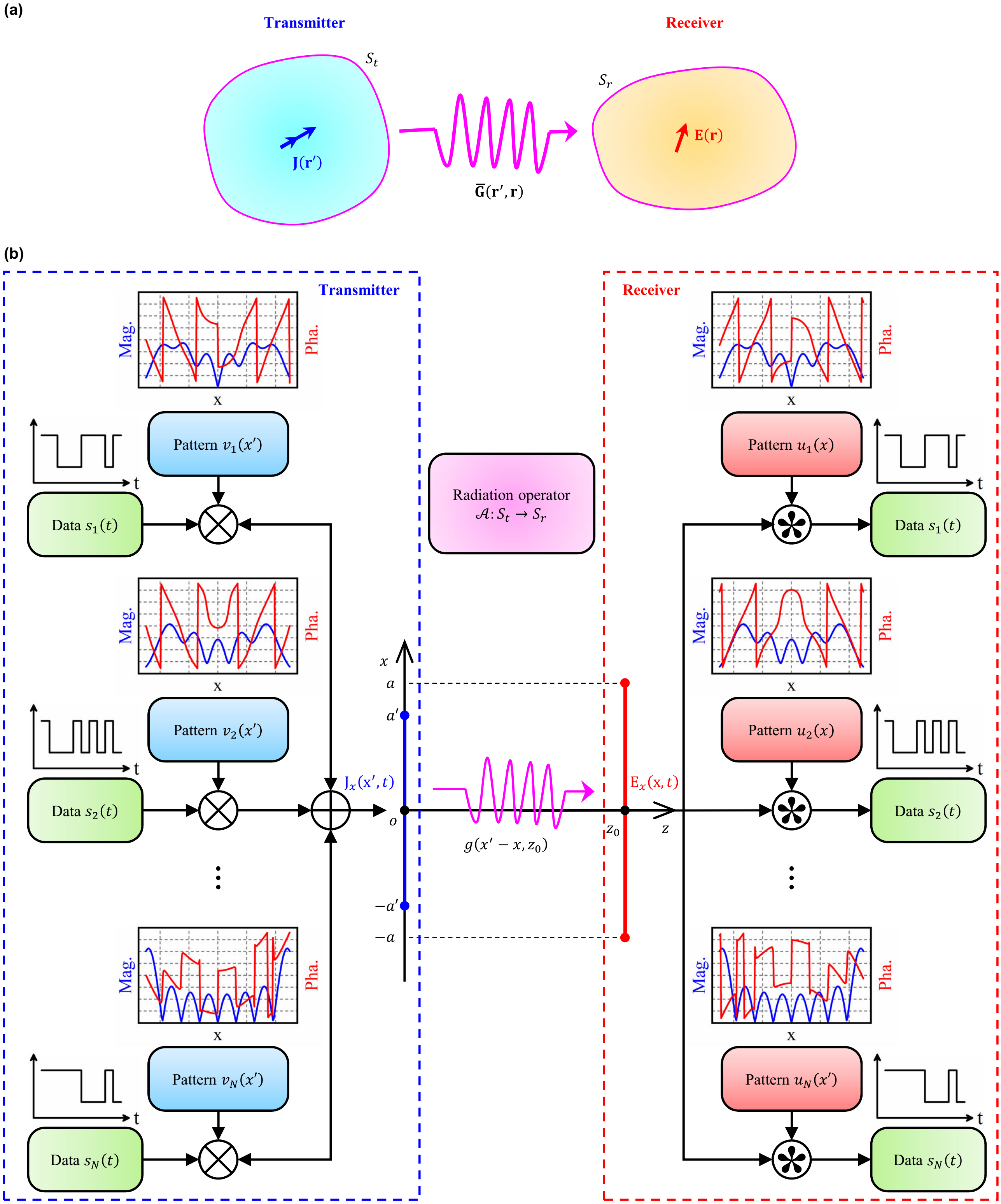

Fig. 2 | The schematic diagrams of holographic MIMO. a The geometry of the 3-D communication problem. **b** The flowchart of the proposed holographic MIMO system.

complicated channel estimation of the holographic MIMO. Then, the baseband information is pre-encoded on the transmitter and combined on the receiver by making the best use of spatial EDoF of aperture fields. Therefore, the scheme requires the transmitter to generate continuous or high-resolution currents on the aperture, which is known as the holographic MIMO. In traditional architecture, the receiver and transmitter consist of antenna arrays, and their element periods are often slightly less than half wavelength, which cannot satisfy the continuous-aperture requirement. However, reducing the spatial period will increase the number of antenna elements rapidly, along with that of active devices such as T/R components. As a result, the high cost, complexity, and power consumption make the holographic MIMO system unfeasible. More importantly, the mutual coupling in antenna arrays will increase rapidly as the element interval decreases, which leads to strong

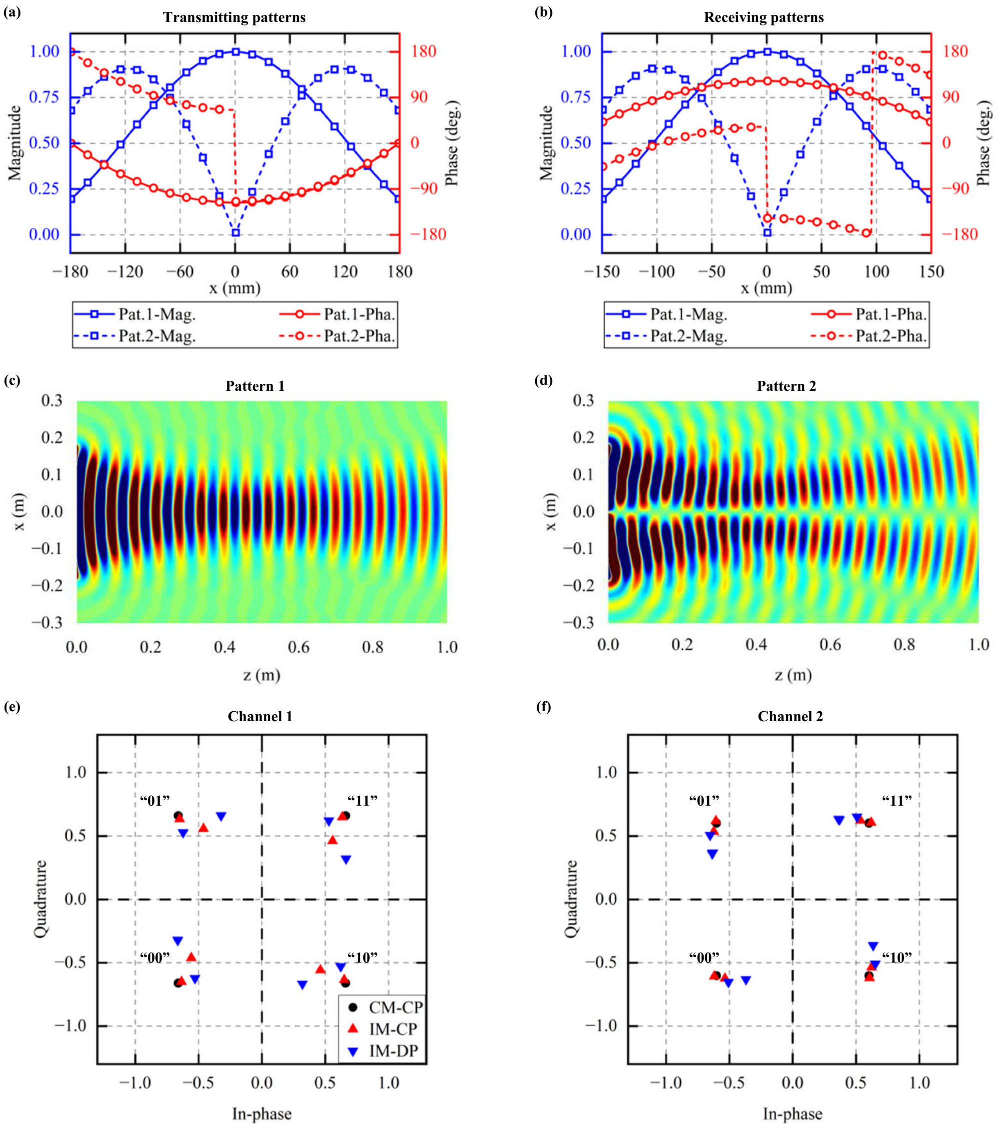

Fig. 3 | Theoretical calculations of the dual-channel holographic MIMO. a, **b** The equivalent current patterns on the transmitting and receiving apertures, in which the blue and red curves represent the magnitude and phase, respectively; the solid and dotted curves represent Patterns 1 and 2, respectively. Here, Pat. is the abbreviation of the pattern. **c**, **d** The propagation modes of Patterns 1 and 2, respectively. **e**, **f** The constellations of QPSK signals transmitted by Channels 1 and 2, respectively. Here, CM-CP, IM-CP and IM-DP are the abbreviations of “continuous magnitude and continuous phase”, “identical magnitude and continuous phase”, and “identical magnitude and 2-bit discrete phase”, respectively.

interference in the communication system. Though some decoupling techniques can reduce these bad influences, they will also increase the system complexity. Therefore, for present schemes, it is difficult and unfeasible to realize the holographic MIMO system directly by reducing the element interval of the antenna array.

As a new technology, PDCM can perform real-time and sub-wavelength-scale modulations on the EM waves at low cost, which makes the holographic MIMO system possible. On the other hand, direct digital modulation (DDM) uses tunable devices on the aperture to transmit information and eliminates mixers and T/R components, which greatly reduces the system cost and complexity. Hence PDCM is an ideal solution for meeting the requirements of the holographic MIMO system. Here, we propose a prototype of the holographic MIMO communication system composed of PDCM and DDM architecture and realize multi-channel signal transmissions under the guidance of EM information theory.

Based on EIT, a system with two EDoFs is designed to verify the multi-channel communication capability of the proposed holographic MIMO. The transmitter is a PDCM consisting of massive 1/4-wavelength 2-bit meta-atoms to achieve high spatial resolution. FPGAs are used to control the coding patterns on PDCM in real-time. The receiver follows the traditional architecture and consists of an antenna array. The array is composed of probe antennas to pick up the electric fields. Software-defined radio (SDR) platform is connected to the probes to demodulate the received information. The system works at 5 GHz and has a transmitter aperture of 360 mm (6λ) and a receiver aperture of 300 mm (5λ). The distance between the transmitting and receiving apertures is 800 mm (about 13.3λ). According to these geometric parameters and Eq. (7), the accurate EDoF of the system is calculated as 2.16 from EIT.

The first two current patterns on the transmitting aperture are obtained by the Hilbert-Schmidt decomposition, as shown in Fig. 3a. The magnitude of the first pattern exhibits a peak shape with a single maximum in the middle, while the second pattern shows double peaks with two identical and symmetrically distributed maxima and one zero point at the center of the aperture. The phases of the two patterns are identical on the left side of the zero point and differ by 180° on the right side. The electric field patterns on the receiving aperture are calculated similarly, as shown in Fig. 3b. The magnitudes of the receiving and transmitting patterns are identical, while the phases exhibit a slight difference. Specifically, the differences between the two patterns on the left and right sides are 90° and -90°, respectively, instead of 0° and 180°. The propagation processes of these two modes are presented in Fig. 3c and d, respectively. We can find that the first mode contains one main beam, while the second one consists of two symmetrical beams with opposite phases. The two modes are very close to the sum and difference beams. However, it is worth noting that the modes are not always similar to the sum and difference beams as the geometric parameters of the system change.

As mentioned in the previous section, each combination of the holographic aperture currents corresponds to one spatial channel. Hence the two patterns in Fig. 3a and b are used to realize dual-channel QPSK signal transmissions. According to Eq. (8), the aperture current is read as

$$\mathrm{J}_x(x') = s_1 \upsilon_1(x') + s_2 \upsilon_2(x') \tag{11}$$

where $s_1, s_2 \in \{e^{j0.25\pi}, e^{j0.75\pi}, e^{j1.25\pi}, e^{j1.75\pi}\}$ are the symbols of QPSK and $\upsilon_1(x')$, $\upsilon_2(x')$ are the transmitting patterns. Overall, there are $4 \times 4 = 16$ patterns, and each one corresponds to a combination of two independent QPSK symbols. The metasurface has limited capability in adjusting the EM wave, particularly in terms of magnitude. Among the available control methods for programmable metasurfaces, the magnitude modulation will significantly increase the complexity and energy consumption of the system. Therefore, we consider the phase-only modulation metasurfaces. Since varactor diodes realize continuous phase modulation, while PIN diodes only achieve discrete phases, we consider three different constraints on the aperture current, namely, continuous magnitude and continuous phase (CM-CP), identical magnitude and continuous phase (IM-CP), and identical magnitude and 2-bit discrete phase (IM-DP). The three constraints correspond to the ideal model, the varactor diode, and the PIN diode, respectively. The current distributions of 16 symbol combinations under different constraints are given in Supplementary Note 1. Figure 3e and f show the received constellations of Channels 1 and 2, respectively. For IM-CP and IM-DP, the constellation points of the same symbols in Channel 1 vary slightly with the symbols transmitted in Channel 2. The same case holds for Channel 2. This phenomenon indicates that there are some interferences between the two channels due to the constraints on the magnitude or phase of the aperture current. However, the constellation points of different symbols are good enough to be distinguished. Therefore, we can still use this system to realize dual-channel communications.

Experimental verifications

In the previous sections, we preliminarily evaluate the feasibility of the holographic MIMO system through theoretical calculations. To further verify the configuration presented in Fig. 3a, a 2-bit phase modulation PDCM is designed for simulations and fabricated for experiments. Based on the designed PDCM, an experimental system is constructed, and the configuration is shown in Fig. 4a. The transmitter consists of the feeding horn, signal source, PDCM, and control platform (FPGA), and the receiver is composed of the probe array and SDR platform (USRP). Considering the practical experimental conditions, the number of SDRs is limited. Thus, only two probe antennas are used as receivers. The processing of the electric fields on the receiving aperture also degenerates into inner products of vector. The probe array and PDCM are aligned in a parallel and coaxial configuration with a separation distance of 800 mm (13.3λ). The receiving aperture has a width of 300 mm (5λ). Two probes are utilized to uniformly sample the electric fields over the aperture, with a distance of 150 mm (2.5λ). The feeding horn is situated at the left front of the metasurface, with a distance of 600 mm (10λ) from the PDCM plane and an axial distance of 300 mm (5λ). The orientation of the feeding horn forms an angle of 30° with respect to the axis. The carrier generated by the source is emitted by the horn antenna and subsequently mixed with the baseband signal imposed on PDCM. The scattered EM signal is finally received by the probe array and demodulated by the SDR platform to obtain the constellation results.

Since the horn antenna is used as excitation, the incident field on PDCM is inhomogeneous, as given in Supplementary Note 2. The actual reflection coefficient distribution on PDCM is obtained by dividing the calculated current pattern by the excited electric field. Then the reflection coefficients are quantized into the four states that the 2-bit PDCM element provides. Through experimental measurements, we find that the performance of the PDCM element is not as ideal as the simulation in Fig. 4b. The measured reflection coefficients are closest to those of the ideal 2-bit metasurface at 4.95 GHz due to parasitic parameters and other factors. Thus, the carrier frequency in the experiments is set to 4.95 GHz instead of the 5 GHz in the simulation. The normalized reflection coefficients of the metasurface element under four coding states are 1, $-0.0966 + 0.9580\mathrm{i}$, $-0.4030 - 0.3280\mathrm{i}$, and $0.0442 - 0.6360\mathrm{i}$, respectively, at 4.95 GHz. To handle the fluctuations in the magnitudes and phases of reflection coefficients, the Euclidean distance minimization criterion is adopted for quantization. In specific, the coding state closest to the theoretical reflection coefficient in the complex plane is chosen as the quantization result, and the detailed strategy is given in Supplementary Note 3.

After considering the incident electric fields of the feeding horn and the practical reflection coefficients of the PDCM element, we can obtain 16 sets of coding distributions on the PDCM that induce two groups of QPSK symbols. The coding distributions are shown in Fig. 4b, where the blue, green, orange and red squares represent the coding states “0”, “1”, “2” and “3”, respectively. Based on the fabricated PDCM sample, a dual-channel holographic MIMO communication system is finally built up according to the coding strategy.

The photograph of the experimental scene is shown in Fig. 5a. The detailed photographs of the PDCM and probe array are provided in the inserted figure. A microwave signal source connected to a linearly-polarized horn antenna serves as the excitation and provides the carrier waves. The desired coding sequences are generated by a control platform (NI PXIe-1082) with a high-speed bus controller, an FPGA module (NI PXIe-7966R), a synchronous clock module (NI PXIe-6674T), and a digital I/O module (NI 6581B), which are then loaded to PDCM through the digital input and output (DIO) lines. On the whole, 48 independent signals are generated to control the 24 columns of 2-bit PDCM elements. An SDR platform (NI USRP-2974) connected with two probes is configured to perform the signal demodulations, including the down-conversion, sampling, and baseband operation. Finally, the transmitted bit streams are recovered, and the real-time constellation results are displayed on the screen, which are straightforward representations of the relation between the baseband signals. Non-line-of-sight (NLOS) experiments are also taken into consideration. As shown in Fig. 5b, a cardboard with a thickness of about 4 cm is placed in front of the probe array to simulate the NLOS propagation, while all other configurations are the same as those in Fig. 5a.

Using the fabricated holographic MIMO hardware, we successfully implement the dual-channel QPSK modulations at the frequency of 4.95 GHz, without needing any channel estimations. The measured constellation diagrams are shown in Fig. 5c and d. Due to the performance limitations of PDCM and environmental factors, the measured constellations are worse than the simulated results presented in Fig. 3e and f. The full-wave simulated scattering patterns of scanning beams by the fabricated PDCM are given in Supplementary Note 4, which can reflect the coupling level. It is the mutual coupling that causes the gap between the calculated and measured constellation diagrams. The constellation points in one channel vary with the symbols transmitted

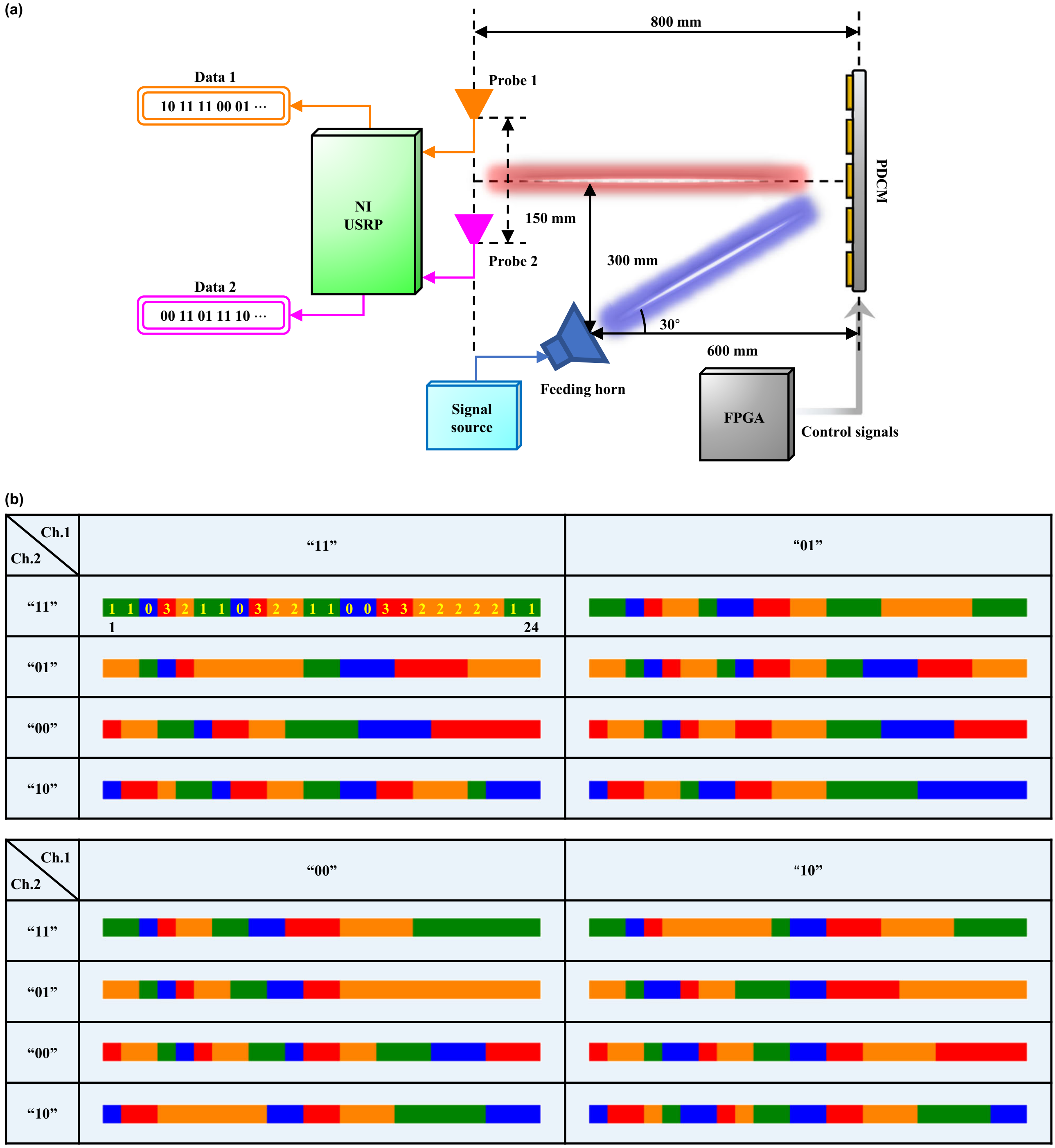

Fig. 4 | Details of the experimental verifications. **a** The schematics of the experimental setup for measurements. **b** The coding distributions on PDCM that induce the dual-channel QPSK symbols. Note that there are 24 columns of elements, and the 16 elements in the same column share the same codes.

in another one. Consequently, there is significant coupling between the two channels. However, the constellation points of the two channels show obvious zoning effect in general, and four QPSK symbols can be clearly distinguished. Moreover, by comparing the blue and red dots in Fig. 5c and d, it can be found that the impact of NLOS propagation on our system is negligible. Overall, a PDCM-based dual-channel holographic MIMO system prototype has been built up and measured. The experiment preliminarily verifies the feasibility of constructing orthogonal channels to transmit information based on the Hilbert-Schmidt decomposition. Some decoupling algorithms and the macroscopic model in ref. 29 may be used to improve the system performance in future research.

Discussion

We proposed a holographic MIMO scheme based on PDCM and EIT, from which, a dual-channel wireless communication system was demonstrated for using spatial diversity and providing direct data transmissions. In the proposed scheme, EIT was used to replace the channel estimation of the holographic MIMO to realize spatial diversity, and PDCM successfully eliminated the requirement for a large number of mixers and T/R components, thus simplifying the system architecture and significantly reducing the cost and power consumption of the holographic MIMO system.

In Table 1, we compare our work with various past pioneering works on PDCMs. The data rate of our system is only next to that in

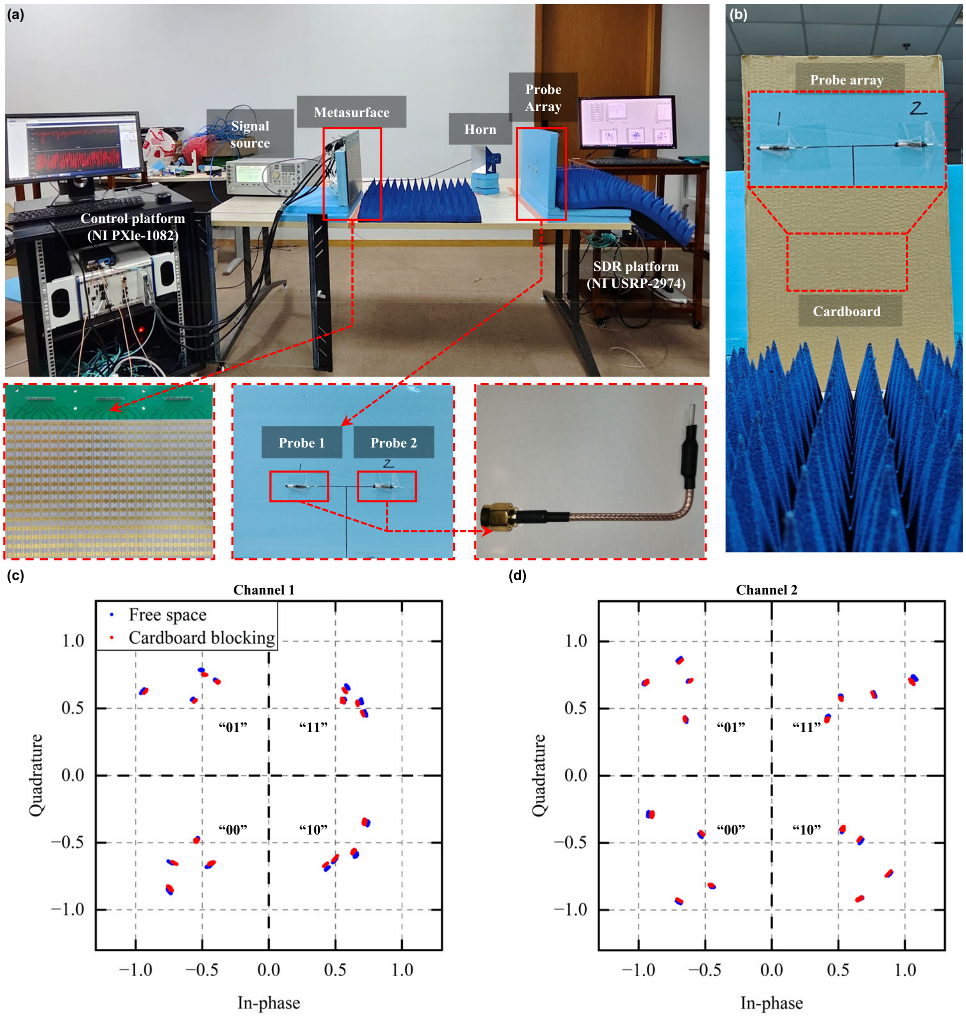

Fig. 5 | Measurements of the near-field PDCM-based holographic MIMO. **a** Photograph of the dual-channel holographic MIMO system based on the 2-bit PDCM and EIT. Details about the metasurface and probe array are provided in the inserted figure. **b** Photograph of the receiver blocked by a cardboard in measurements. **c**, **d** The measured constellation diagrams of Channels 1 and 2, respectively. The blue and red dots represent the systems working in free space and with the cardboard blocking, respectively.

Table 1 | Comparison with the previous PDCM-based communication system

	Ref. 56	Ref. 57	Ref. 58	Ref. 59	Ref. 60	Ref. 61	Our work
Carrier frequency	3.6 GHz	4 GHz	10 GHz	9.5 GHz	29 GHz	2.7 GHz	4.95 GHz
Aperture size	3.48λ × 3.09λ	3.37λ × 2.34λ	6.67λ × 6.67λ	7.09λ × 3.55λ	7.06λ × 5.04λ	4.88λ × 3.69λ	5.94λ × 3.96λ
Tunable device	varactor	varactor	PIN	PIN	PIN	varactor	PIN
Phase range	2-bit	2-bit	1-bit	2-bit	1-bit	0 ~ 180°	2-bit
Modulation method	BFSK	QPSK	OOK	OOK	256QAM	16PSK	QPSK
Distance	Far-field	Far-field	Near-field	Far-field	Far-field	Far-field	Near-field
Bit rate	78.125 kbps	1.6384 Mbps	500 kbps	2.5 Mbps	1.25 Mbps	20 Mbps	4 Mbps
Number of user	1	1	3	2	1	1	1
Number of channel for one user	1	1	1	1	1	2	2
Multiplexing method	–	–	Space	Space-frequency	–	Polarization-frequency	Space

ref. 61. Unlike previous works, our method focuses on using spatial diversity to increase the number of single-user channels. In previous works, polarization and frequency diversities are used to increase the number of channels[59,61], while spatial one is more inclined to achieve multi-user[58,59]. In ref. 58, the maximum distance between the receiving antennas is 492 mm (corresponding to 15λ). In ref. 59, the angle between the receiving antennas is 60°. Both are unavailable for single-user in real communication scenarios. In contrast, these two values in our work are 2.475λ and 10°, respectively, which is more reasonable for single-user to make full use of the receiving aperture. Therefore, our work is an extension of the PDCM-based communication system in a new dimension. At the same time, it can also be combined with various multiplexing methods in these previous works to realize a multi-user, multi-channel wireless communication architecture[32].

Although the system only has 2 EDoFs in the microwave range, it can be extended to more EDoFs at higher frequencies such as

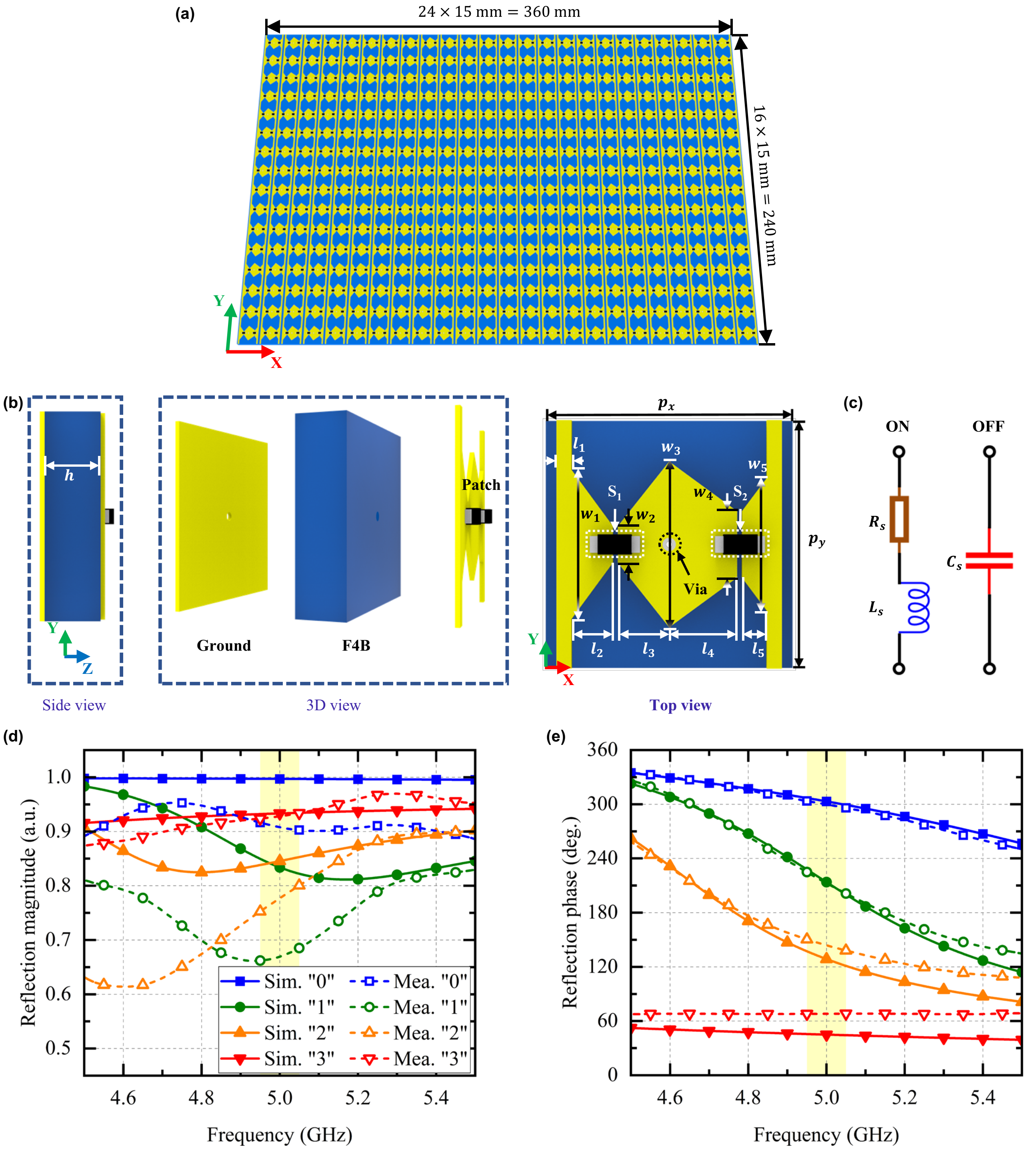

Fig. 6 | Details of the 2-bit phase modulation PDCM. **a** The schematic view of the designed 2-bit PDCM with 24 × 16 elements. **b** The side, 3D, and top views of the element loaded with two PIN diodes. **c** The equivalent circuit models of the PIN diode biased at the "ON" and "OFF" states. **d**, **e** The magnitudes and phases of the reflection coefficients of the element under the four combinations of the diode states. Sim. and Mea. are the abbreviations of simulation and measurement, respectively. The "0", "1", "2" and "3" represent the diode states as "OFF-OFF", "OFF-ON", "ON-OFF" and "ON-ON", respectively.

millimeter waves and terahertz waves. Meanwhile, the scattering and diffraction of the millimeter-wave channels are much smaller, which is more consistent with the free-space assumption in EIT. The proposed PDCM-based holographic MIMO system provides a low-cost, low-power, and low-complexity solution to exploit the increased spatial EDoFs brought by the growing frequency of future wireless communications. It is noted that the potential of PDCM in the temporal and spatial modulations has not been fully utilized in the present system. It could be greatly enhanced if the PDCM and various signal processing techniques are deeply integrated. We believe that our research establishes a solid foundation for the holographic MIMO techniques in future 6G wireless communications.

Methods

Details on the 2-bit phase modulation PDCM

The PDCM designed for experimental verifications is shown in Fig. 6a. It consists of 24 × 16 elements and has an overall size of

360 × 240 mm^2 (6 × 4 λ^2). The 16 coding elements in each column share a common control signal. The size of the element is 15 × 15 mm^2, corresponding to 0.25 × 0.25 λ^2. As illustrated in Fig. 6b, each element consists of a pentagonal metal patch and two biasing lines printed on an F4B substrate with dielectric constant 2.65, loss tangent 0.001, and thickness 2 mm. There is a metal via in the middle of the pentagonal patch to connect with ground. Two PIN diodes (SMP-1320) are employed to connect the pentagonal metal with two biasing lines. The geometric parameters of the element are designed to attain 90° phase difference when two PIN diodes are switched among "OFF-OFF", "OFF-ON", "ON-OFF" and "ON-ON", corresponding to the four coding states "0", "1", "2" and "3", respectively. The design details are given in Supplementary Note 5. Full-wave simulations are carried out using the CST Microwave Studio. In the simulations, periodic boundary conditions are applied along the x and y-directions, and two Floquet ports are used along the $+z$ and $-z$-directions. A normally incident plane-wave illumination with an x-polarized electric field is assumed to calculate the reflection coefficients. As shown in Fig. 6c, the equivalent circuit model of the PIN diode is $R_s = 7.8\,\Omega$, $C_s = 28$ pF, and $L_s = 30$ pH around the designed frequency of 5 GHz. The magnitudes and phases of the simulated and measured reflection coefficients under the "0", "1", "2" and "3" states are shown in Figs. 6d and e, in which the "0", "1", "2" and "3" represent the diode states as "OFF-OFF", "OFF-ON", "ON-OFF" and "ON-ON", respectively. We observe that the simulated phase difference between adjacent digital states is about 90°, and the corresponding magnitudes exceed 0.81 at the frequency of 5 GHz. However, the measured reflection coefficient performance deteriorates: the phase differences at 5 GHz are 87°, 69°, 75° and 128°, respectively. After frequency sweeping, we choose 4.95 GHz as the experimental frequency with a smaller standard deviation of the phase difference, in which the phase differences are 80°, 75°, 83°, and 120°, and the minimum magnitude is about 0.66.

Data availability

The data that support the findings of this study is presented in the paper and Supplementary information file.

Code availability

The codes that support the dual-channel near-field holographic MIMO scheme are available from the corresponding author upon request.

References

1. Akyildiz, I. F., Han, C. & Nie, S. Combating the distance problem in the millimeter wave and terahertz frequency bands. *IEEE Commun. Mag.* **56**, 102–108 (2018).
2. Yang, P. et al. 6G wireless communications: Vision and potential techniques. *IEEE Netw.* **33**, 70–75 (2019).
3. Di Renzo, M. et al. Smart radio environments empowered by reconfigurable AI meta-surfaces: An idea whose time has come. *EURASIP J. Wirel. Commun. Netw.* **2019**, 1–20 (2019).
4. Hu, S., Rusek, F. & Edfors, O. Beyond massive MIMO: The potential of positioning with large intelligent surfaces. *IEEE Trans. Signal Process.* **66**, 1761–1774 (2018).
5. Huang, C. et al. Holographic MIMO surfaces for 6G wireless networks: Opportunities, challenges, and trends. *IEEE Wirel. Commun.* **27**, 118–125 (2020).
6. Dardari, D. & Decarli, N. Holographic communication using intelligent surfaces. *IEEE Commun. Mag.* **59**, 35–41 (2021).
7. Deng, R. et al. Reconfigurable holographic surface-enabled multi-user wireless communications: Amplitude-controlled holographic beamforming. *IEEE Tran. Wirel. Commun.* **21**, 6003–6017 (2022).
8. Gong, T. et al. Holographic MIMO communications: Theoretical foundations, enabling technologies, and future directions. *IEEE Communications Surveys & Tutorials* **26**, 195–257 (2023).
9. Bucci, O. M. & Franceschetti, G. On the spatial bandwidth of scattered fields. *IEEE Trans. Antennas Propag.* **35**, 1445–1455 (1987).
10. Bucci, O. M. & Franceschetti, G. On the degrees of freedom of scattered fields. *IEEE Trans. Antennas Propag.* **37**, 918–926 (1989).
11. Pierri, R. & Soldovieri, F. On the information content of the radiated fields in the near zone over bounded domains. *Inverse Probl.* **14**, 321 (1998).
12. Telatar, E. Capacity of multi-antenna Gaussian channels. *Eur. Trans. Telecommun.* **10**, 585–595 (1999).
13. Poon, A. S., Brodersen, R. W. & Tse, D. N. C. Degrees of freedom in multiple-antenna channels: A signal space approach. *IEEE Trans. Inf. Theory* **51**, 523–536 (2005).
14. Gruber, F. K. & Marengo, E. A. New aspects of electromagnetic information theory for wireless and antenna systems. *IEEE Trans. Antennas Propag.* **56**, 3470–3484 (2008).
15. Jensen, M. A. & Wallace, J. W. Capacity of the continuous-space electromagnetic channel. *IEEE Trans. Antennas Propag.* **56**, 524–531 (2008).
16. Migliore, M. D. On electromagnetics and information theory. *IEEE Trans. Antennas Propag.* **56**, 3188–3200 (2008).
17. Wan, Z. et al. Mutual information for electromagnetic information theory based on random fields. *IEEE Trans. Commun.* **71**, 1982–1996 (2023).
18. Li, R. et al. An electromagnetic information theory based model for efficient characterization of MIMO systems in complex space. *IEEE Trans. Antennas Propag.* **71**, 3497–3508 (2023).
19. Ji, R. et al. Extra DoF of near-field holographic MIMO communications leveraging evanescent waves. *IEEE Wirel. Commun. Lett.* **12**, 580–584 (2023).
20. Yuan, S. S. A. et al. Effects of mutual coupling on degree of freedom and antenna efficiency in holographic MIMO communications. *IEEE Open J. Antennas Propag.* **4**, 237–244 (2023).
21. Pendry John Brian. Negative refraction makes a perfect lens. *Phys. Rev. Lett.* **85**, 3966 (2000).
22. Yu, N. et al. Light propagation with phase discontinuities: generalized laws of reflection and refraction. *Science* **334**, 333–337 (2011).
23. Glybovski, S. B. et al. Metasurfaces: From microwaves to visible. *Phys. Rep.* **634**, 1–72 (2016).
24. Sun, S. et al. High-efficiency broadband anomalous reflection by gradient meta-surfaces. *Nano Lett.* **12**, 6223–6229 (2012).
25. Cui, T. J. et al. Coding metamaterials, digital metamaterials and programmable metamaterials. *Light Sci. Appl.* **3**, e218–e218 (2014).
26. Cui, T. J., Liu, S. & Zhang, L. Information metamaterials and metasurfaces. *J. Mater. Chem. C* **5**, 3644–3668 (2017).
27. Cui, T. J. et al. Information metamaterial systems. *Iscience* **23**, 101403 (2020).
28. Wang, Z. X. et al. A long-range and nearly passive RFID-controlled information metasurface. *Adv. Opt. Mater.* **12**, 2203114 (2024).
29. Shao, R. W. et al. Macroscopic model and statistical model to characterize electromagnetic information of a digital coding metasurface. *Natl. Sci. Rev.* **11**, nwad299 (2024).
30. Yang, H. Q. et al. Complex matrix equation solver based on computational metasurface. *Adv. Funct. Mater.* **34**, 2310234 (2023).
31. Wang, Z. X. et al. A low-cost and low-profile electronically programmable bit array antenna for two-dimensional wide-angle beam steering. *IEEE Trans. Antennas Propag.* **71**, 342–352 (2022).

32. Xu, H. et al. Two-dimensional and high-order directional information modulations for secure communications based on programmable metasurface. *Nat. Commun.* **15**, 6140 (2024).
33. Wu, J. et al. Realizing complex beams via amplitude-phase digital coding metasurfaces and semidefinite relaxation optimization. *Front. Inf. Technol. Electron. Eng.* **24**, 1708–1716 (2023).
34. Huang, C. et al. Reconfigurable intelligent surfaces for energy efficiency in wireless communication. *IEEE Trans. Wirel. Commun.* **18**, 4157–4170 (2019).
35. Basar, E. et al. Wireless communications through reconfigurable intelligent surfaces. *IEEE Access* **7**, 116753–116773 (2019).
36. Wu, Q. & Zhang, R. Intelligent reflecting surface enhanced wireless network via joint active and passive beamforming. *IEEE Trans. Wirel. Commun.* **18**, 5394–5409 (2019).
37. Liu, R. et al. A path to smart radio environments: An industrial viewpoint on reconfigurable intelligent surfaces. *IEEE Wirel. Commun.* **29**, 202–208 (2022).
38. Dai, L. et al. Reconfigurable intelligent surface-based wireless communications: Antenna design, prototyping, and experimental results. *IEEE Access* **8**, 45913–45923 (2020).
39. Pei, X. et al. RIS-aided wireless communications: Prototyping, adaptive beamforming, and indoor/outdoor field trials. *IEEE Trans. Commun.* **69**, 8627–8640 (2021).
40. Basar, E. et al. Reconfigurable Intelligent Surfaces for 6G: Emerging Hardware Architectures, Applications, and Open Challenges. *IEEE Veh. Technol. Mag.* **19**, 27–47 (2024).
41. Huang, C., Mo, R. & Yuen, C. Reconfigurable intelligent surface assisted multiuser MISO systems exploiting deep reinforcement learning. *IEEE J. Sel. Areas Commun.* **38**, 1839–1850 (2020).
42. An, J. et al. Stacked intelligent metasurface-aided MIMO transceiver design. *IEEE Wirel. Commun.* **31**, 123–131 (2024).
43. Liu, B. et al. Multifunctional vortex beam generation by a dynamic reflective metasurface. *Adv. Opt. Mater.* **9**, 2001689 (2021).
44. Jiang, M. et al. Efficient and accurate simulations of metamaterials based on domain decomposition and unit feature database. *IEEE Trans. Antennas and Propagation.* **72**, 8635–8646 (2024).
45. Shao, H. et al. A fast model order reduction method for electromagnetic scattering of large periodic arrays with connected elements. *IEEE Trans. Antennas Propag.* **71**, 9142–9147 (2023).
46. Zhang, L. et al. Space-time-coding digital metasurfaces. *Nat. Commun.* **9**, 4334 (2018).
47. Dai, J. Y. et al. Independent control of harmonic amplitudes and phases via a time-domain digital coding metasurface. *Light Sci. Appl.* **7**, 90 (2018).
48. Zhang, C. et al. Convolution operations on time-domain digital coding metasurface for beam manipulations of harmonics. *Nanophotonics* **9**, 2771–2781 (2020).
49. Ke, J. C. et al. Linear and nonlinear polarization syntheses and their programmable controls based on anisotropic time-domain digital coding metasurface. *Small Structures* **2**, 2000060 (2021).
50. Ramaccia, D. et al. Phase-induced frequency conversion and Doppler effect with time-modulated metasurfaces. *IEEE Trans. Antennas Propag.* **68**, 1607–1617 (2019).
51. Wu, Z. & Grbic, A. Serrodyne frequency translation using time-modulated metasurfaces. *IEEE Trans. Antennas Propag.* **68**, 1599–1606 (2019).
52. Liu, M., Kozyrev, A. B. & Shadrivov, I. V. Time-varying metasurfaces for broadband spectral camouflage. *Phys. Rev. Appl.* **12**, 054052 (2019).
53. Cui, T. J. et al. Direct transmission of digital message via programmable coding metasurface. *Research* **2019**, 2584509 (2019).
54. Tang, W. et al. Path loss modeling and measurements for reconfigurable intelligent surfaces in the millimeter-wave frequency band. *IEEE Trans. Commun.* **70**, 6259–6276 (2022).
55. Cheng, Q. et al. Reconfigurable intelligent surfaces: Simplified-architecture transmitters—From theory to implementations. *Proc. IEEE* **110**, 1266–1289 (2022).
56. Zhao, J. et al. Programmable time-domain digital-coding metasurface for non-linear harmonic manipulation and new wireless communication systems. *Natl. Sci. Revi.* **6**, 231–238 (2019).
57. Dai, J. Y. et al. Wireless communications through a simplified architecture based on time-domain digital coding metasurface. *Adv. Mater. Technol.* **4**, 1900044 (2019).
58. Wan, X. et al. Multichannel direct transmissions of near-field information. *Light Sci. Appl.* **8**, 60 (2019).
59. Zhang, L. et al. A wireless communication scheme based on space- and frequency-division multiplexing using digital metasurfaces. *Nat. Electron.* **4**, 218–227 (2021).
60. Chen, M. Z. et al. Accurate and broadband manipulations of harmonic amplitudes and phases to reach 256 QAM millimeter-wave wireless communications by time-domain digital coding metasurface. *Natl. Sci. Rev.* **9**, nwab134 (2022).
61. Ke, J. C. et al. Space-frequency-polarization-division multiplexed wireless communication system using anisotropic space-time-coding digital metasurface. *Natl. Sci. Rev.* **9**, nwac225 (2022).

Acknowledgements

This work was supported by the National Key Research and Development Program of China (2021YFA1401002), the National Natural Science Foundation of China (62288101, 62171124, 62225108, 62261160576 and 62201138), the Jiangsu Province Frontier Leading Technology Basic Research Project (BK20212002), the School Discipline Innovation Talent Recruitment Program (111-2-05), the Fundamental Research Funds for the Central Universities (2242024K30009), the Key Technologies R&D Program of Jiangsu (Prospective and Key Technologies for Industry) (BE2023022-1 and BE2023022) and the Jiangsu Provincial Innovation and Entrepreneurship Doctor Program.

Author contributions

T.J.C., J.W.W., S.J., and Q.C. conceived the idea and revised the manuscript. R.W.S. and J.W.W. carried out the theoretical analysis and developed the scheme of the system. R.W.S. and Z.X.W. built the digital coding metasurface and conducted the proof-of-principle experiments. J.L., S.M., R.W.S., Y.X., and W.T. designed the software and conducted the communication experiments. R.W.S. wrote the manuscript. All authors revised this paper.

Competing interests

The authors declare no competing interests.

Additional information

Supplementary information The online version contains supplementary material available at https://doi.org/10.1038/s41467-025-56209-x.

Correspondence and requests for materials should be addressed to Shi Jin or Tie Jun Cui.

Peer review information *Nature Communications* thanks Xinyuan Fang, and the other anonymous reviewer(s) for their contribution to the peer review of this work. A peer review file is available.